Engineering Analysis with Boundary Elements 120 (2020) 211–222

Contents lists available at ScienceDirect

Engineering Analysis with Boundary Elements

journal homepage: www.elsevier.com/locate/enganabound

Analysis of transient wave propagation in inhomogeneous media using edge-based gradient smoothing technique and bathe time integration method

Yingbin Chai [a], Zhixiong Gong [b,c], Wei Li [b,c], Yongou Zhang [a,*]

[a] School of Transportation, Wuhan University of Technology, Wuhan 430070, China
[b] School of Naval Architecture and Ocean Engineering, Huazhong University of Science and Technology, Wuhan, Hubei 430074, China
[c] Collaborative Innovation Center for Advanced Ship and Deep-Sea Exploration (CISSE), Shanghai 200240, China

ARTICLE INFO

Keywords:
Wave propagation
Gradient smoothing technique
Bathe time integration
Numerical error
Numerical methods

ABSTRACT

As is known to all, the classical finite element method (FEM) always fails to effectively solve the wave problems in the relatively large wave numbers due to the troublesome numerical error issue. In this paper, the standard FEM with edge-based gradient smoothing technique and Bathe time integration method is developed to analyze the transient wave propagation problems in inhomogeneous media. We explicitly show that the numerical error of the calculated solutions for transient wave propagation problems consists of two different parts, namely the spatial discretization error and the temporal discretization error. Due to the edge-based gradient smoothing technique and the appropriate numerical dissipation effects from Bathe time integration scheme, it is found that the total numerical error can be significantly suppressed and more accurate numerical solutions can be obtained. Several typical numerical examples have been conducted to examine the capacity of the proposed method in solving transient wave propagation problems in inhomogeneous media.

1. Introduction

Despite the great success of the classical finite element method (FEM) in various engineering applications [1–3], so far there still exists several unsolved problems for the FEM. Among them, one well-known intractable problem is the simulation of the short wavelength (high frequency) in wave propagation problems. Due to the particularity of the differential operator in the governing equation for waves, the corresponding finite element (FE) solutions always suffer from the troublesome numerical error issue [4–8].

Actually, the total numerical error of the numerical solutions for transient wave propagation problems mainly consists of two different parts, the first part is the spatial discretization error which is related to the spatial discretization (namely the used mesh pattern) and the second part is the temporal discretization error which is mainly from the used time integration scheme [9]. When the classical finite element method is employed to solve the transient wave propagation problems, the magnitude of the above mentioned numerical dispersion error will expand and accumulate quickly with the increase of the considered wave number and time. In consequence, the accuracy of the numerical solutions can be severely ruined and the obtained numerical results usually become very erroneous [10–12]. In addition, the finite element solutions of transient wave propagation problems also suffer from the troublesome "numerical anisotropy" issue [9], that is the accuracy of the calculated solutions severely depends on the wave propagation directions even if the medium is isotropic and the employed mesh is uniform. When the low order linear element is used, this effect will be even more severe.

In addition to the classical finite element method, there are also many other different numerical techniques can be successfully used to tackle the transient wave propagation problems, such as the boundary element [13,14] or boundary-type discretization techniques [15–21], meshfree method [22–29], spectral element method [30,31], mass-redistributed FEM [32–34] and several other hybrid numerical methods [35–39]. Although these numerical techniques can relieve the numerical error issue to a certain extent and improve the quality of the numerical solution for wave propagation problems. However, the numerical error can still not be completely removed and all of these methods also have their own weakness and conditions of applicability. For example, the standard boundary element approach always result in the non-symmetric and dense system matrices, so more storage requirements and computational cost are also required [40]. The meshfree methods usually need relatively expensive numerical integration and several extra crucial parameters (such as the influence domain, the weight functions, the function bases and so on) usually should be carefully determined [41,42]. The spectral element method are very effective to control the

* Corresponding author.
E-mail addresses: hustcyb@hust.edu.cn (Y. Chai), zhangyo@whut.edu.cn (Y. Zhang).

https://doi.org/10.1016/j.enganabound.2020.08.018
Received 31 March 2020; Received in revised form 7 July 2020; Accepted 29 August 2020

numerical error for one-dimensional wave propagation problems, but it still has difficulties in solving general two- and three-dimensional problems in complex geometries [30,31]. To the authors' best knowledge, there still exists no ideal numerical approach to perfectly solve the transient wave propagation problem, and this is still a very challenging issue in modern computation acoustics [43].

In recent years, the smoothed finite element method (S-FEM) have been proposed to solve various engineering problems [44–51]. The S-FEM is formulated by combining the standard FEM with the gradient smoothing technique (GST) from the meshfree method. Due to the "softening effects" from the GST, S-FEM can provide a softer and appropriate system stiffness which is closer to the real stiffness of the considered system than the standard FEM. It is found that S-FEM can significantly reduce the numerical error in acoustic analysis and produce more accurate numerical solutions than the traditional FEM [52–55]. However, most of the previous published papers mainly focus on investigating the abilities and behaviors of the S-FEM in solving steady-state acoustic wave problems in which the time integration is not considered. Whether the S-FEM also behaves very well in solving transient wave problems is still unclear so far. The present work tries to meet this need and makes attempt to examine the performance of the S-FEM in solving transient wave propagation problems in inhomogeneous media.

In this paper, the edge-based S-FEM, which combines the standard FEM with the edge-based GST, is employed for spatial discretization to solve the transient wave propagation problems in inhomogeneous media. Note that there always exists relatively large spatial discretization error in the relatively large wave number range, the obtained short wavelength modes (or high frequency wave modes) are always inaccurate and then the total solution might be unreliable. For the considered transient wave propagation problems in this work, the Bathe time integration scheme will be used for temporal discretization. One important property of the Bathe time integration method is that there exists appropriate numerical dissipation effects and the above-mentioned inaccurate short wavelength modes can be effectively suppressed, hence very accurate numerical solutions can be always reached for transient wave propagations. In this work we will detailedly investigate the different numerical dispersion error components in solving transient wave propagation problem. It is explicitly shown that the spatial discretization error and temporal discretization error always appear together and affect each other in transient wave analysis.

The present paper is structured as follows: Section 2 presents the fundamental formulation of the transient wave in inhomogeneous media. The detailed formulation of the edge-based gradient smoothing technique in inhomogeneous media is shown in Section 3. Section 4 includes the dispersion analysis of the present approach for transient wave problems. A number of supporting numerical experiments and the related conclusions are then summarized in the remaining sections.

2. Formulation of the transient wave propagation in inhomogeneous media

As shown in Fig. 1, the considered problem domain Ω consists of two sub-domains Ω_1 and Ω_2 with two different media, namely $\Omega = \Omega_1 \cup \Omega_2$, Γ is the interface of the two different media and Γ_N is the imposed Neumann boundary condition. $\mathbf{n}_1$ and $\mathbf{n}_2$ represent the outward unit normals corresponding to Ω_1 and Ω_2, respectively.

For the basic transient wave problems, the corresponding governing equation can be given by [56]

$$\begin{cases} \nabla^2 u_1 - \frac{1}{c_1^2}\ddot{u}_1 = 0, \text{in}\Omega_1 \\ \nabla^2 u_2 - \frac{1}{c_2^2}\ddot{u}_2 = 0, \text{in}\Omega_2 \end{cases} \tag{1}$$

in which ∇^2 is the Laplace operator, u_1 and u_2 are the solution variables (such as displacements), c_1 and c_2 are the wave speed in different media, the overdot denotes the derivative with respect to time.

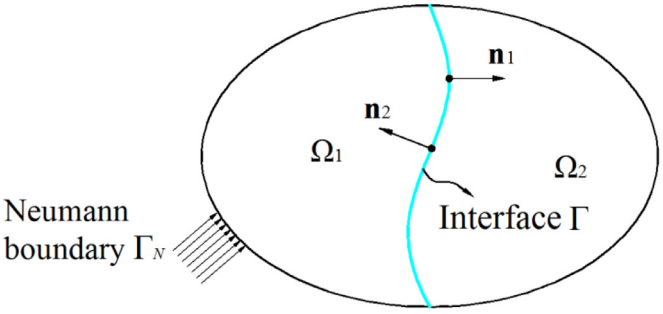

Fig. 1. General problem domain with different media.

On the interface Γ of the different media, the following boundary conditions should be satisfied

$$u_1 = u_2 \tag{2}$$

$$v_1 = v_2 \tag{3}$$

in which v_1 and v_2 denote the normal particle velocities on the interface Γ for two different media.

Based on the general principle of virtual work, the governing equations in Eq. (1) can be written by

$$\sum_{i=1}^{2} \int_{\Omega_i} \bar{u}(\nabla^2 u_i - \frac{1}{c_i^2}\ddot{u}_i) d\Omega = 0 \tag{4}$$

in which $\bar{u}$ denotes any arbitrary "virtual displacement distributions".

By using the divergence theorem and integrating by parts, we have

$$\sum_{i=1}^{2} \left(\int_{\Omega_i} \nabla\bar{u} \cdot \nabla u_i \mathrm{d}\Omega + \frac{1}{c_i^2} \int_{\Omega_i} \bar{u}\ddot{u}_i \mathrm{d}\Omega - \int_{\Gamma_N} \bar{u}(\nabla u_i \cdot \mathbf{n}_i)\mathrm{d}\Gamma \right) = 0 \tag{5}$$

It is known that the specific constraints in Eq. (2) can be achieved in the assemblage of the related system matrices. Here the constraint shown in Eq. (3) is imposed by using the well-known Lagrange multiplier method [1], then we can obtain

$$\Pi^* = \Pi - \int_{\Gamma} \lambda(v_1 + v_2)\mathrm{d}\Gamma \tag{6}$$

in which Π is the original total potential energy, Π^* is the new defined energy functional in which the extra constraints shown in Eq. (3) is considered, λ is the Lagrange multiplier.

By invoking $\delta\Pi^*$=0 and using the standard finite element interpolation [1], we can obtain the following matrix equations

$$\begin{cases} \frac{1}{c_1^2}\int_{\Omega_1} \mathbf{N}_{f_1}^T \mathbf{N}_{f_1} \ddot{\mathbf{u}}_1 \mathrm{d}\Omega + \int_{\Omega_1} \left(\nabla \mathbf{N}_{f_1}\right)^T \nabla \mathbf{N}_{f_1} \mathbf{u}_1 \mathrm{d}\Omega - \int_{\Gamma_N} \mathbf{N}_{f_1}^T (\nabla p_1 \cdot \mathbf{n}_1)\mathrm{d}\Gamma - \int_{\Gamma} \\ \quad \left(\nabla \mathbf{N}_{f_1}\right)^T \mathbf{n}_1 \mathbf{N}_\lambda c_1 \lambda \mathrm{d}\Gamma = 0 \\ \frac{1}{c_2^2}\int_{\Omega_2} \mathbf{N}_{f_2}^T \mathbf{N}_{f_2} \ddot{\mathbf{u}}_2 \mathrm{d}\Omega + \int_{\Omega_2} \left(\nabla \mathbf{N}_{f_2}\right)^T \nabla \mathbf{N}_{f_2} \mathbf{u}_2 \mathrm{d}\Omega - \int_{\Gamma_N} \mathbf{N}_{f_2}^T (\nabla p_2 \cdot \mathbf{n}_2)\mathrm{d}\Gamma \\ \quad - \int_{\Gamma} \left(\nabla \mathbf{N}_{f_2}\right)^T \mathbf{n}_2 \mathbf{N}_\lambda c_2 \lambda \mathrm{d}\Gamma = 0 \\ - \int_{\Gamma} \mathbf{N}_\lambda \mathbf{n}_1 \left(\nabla \mathbf{N}_{f_1}\right)^T c_1 \mathbf{u}_1 \mathrm{d}\Gamma - \int_{\Gamma} \mathbf{N}_\lambda \mathbf{n}_2 \left(\nabla \mathbf{N}_{f_2}\right)^T c_2 \mathbf{u}_2 \mathrm{d}\Gamma = 0 \end{cases} \tag{7}$$

in which $\mathbf{N}_{f_1}$, $\mathbf{N}_{f_2}$ and $\mathbf{N}_\lambda$ are the nodal interpolation functions corresponding to the two different sub-domains (Ω_1 and Ω_2) and the interface Γ, $\mathbf{u}_1$, $\mathbf{u}_2$ and λ are the solution variables need to be calculated.

The above matrix equations can be further simplified by

$$\begin{bmatrix} \mathbf{M}_1 & \mathbf{0} & \mathbf{0} \\ \mathbf{0} & \mathbf{M}_2 & \mathbf{0} \\ \mathbf{0} & \mathbf{0} & \mathbf{0} \end{bmatrix} \begin{bmatrix} \ddot{\mathbf{p}}_1 \\ \ddot{\mathbf{p}}_2 \\ \ddot{\boldsymbol{\lambda}} \end{bmatrix} + \begin{bmatrix} \mathbf{K}_1 & \mathbf{0} & \mathbf{A} \\ \mathbf{0} & \mathbf{K}_2 & \mathbf{G} \\ \mathbf{A}^T & \mathbf{G}^T & \mathbf{0} \end{bmatrix} \begin{bmatrix} \mathbf{p}_1 \\ \mathbf{p}_2 \\ \boldsymbol{\lambda} \end{bmatrix} = \begin{bmatrix} \mathbf{R}_1 \\ \mathbf{R}_2 \\ \mathbf{0} \end{bmatrix} \tag{8}$$

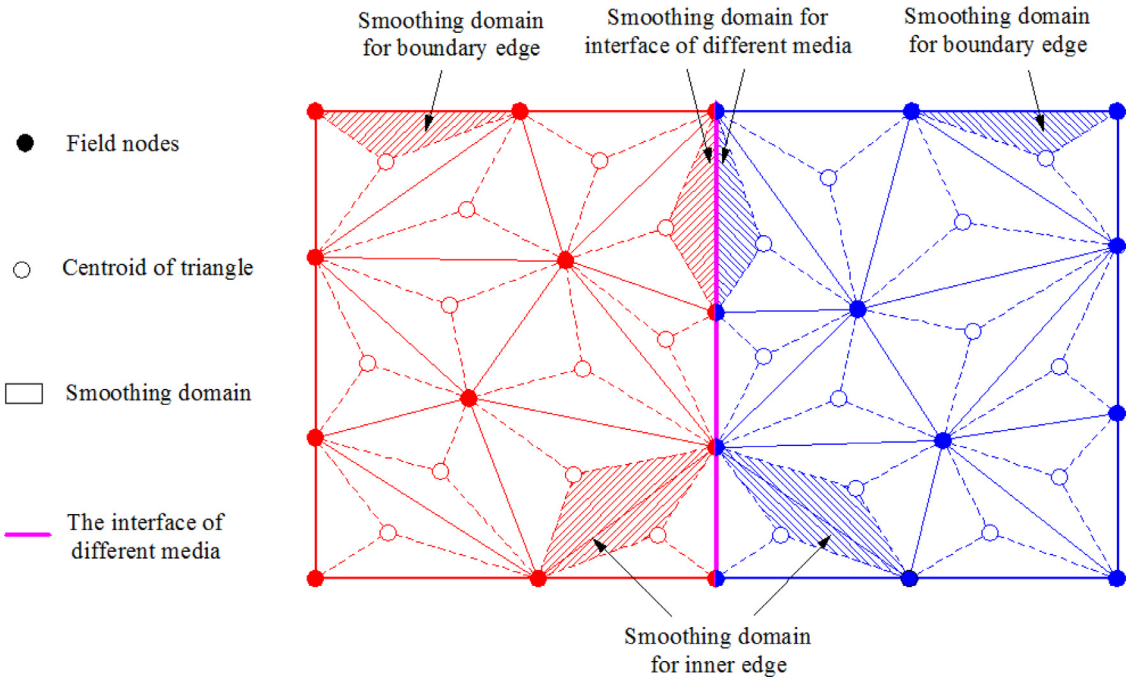

Fig. 2. The edge-based smoothing domains in the problem domain with different materials.

in which

$$\begin{aligned}&\mathbf{M}_1 = \frac{1}{c_1^2}\int_{\Omega_1}\mathbf{N}_{f_1}^T\mathbf{N}_{f_1}\mathrm{d}\Omega, \mathbf{M}_2 = \frac{1}{c_2^2}\int_{\Omega_2}\mathbf{N}_{f_2}^T\mathbf{N}_{f_2}\mathrm{d}\Omega\\&\mathbf{K}_1 = \int_{\Omega_1}\left(\nabla\mathbf{N}_{f_1}\right)^T\nabla\mathbf{N}_{f_1}\mathrm{d}\Omega, \mathbf{K}_2 = \int_{\Omega_2}\left(\nabla\mathbf{N}_{f_2}\right)^T\nabla\mathbf{N}_{f_2}\mathrm{d}\Omega\\&\mathbf{A} = -\int_{\Gamma}\left(\nabla\mathbf{N}_{f_1}\right)^T\mathbf{n}_1\mathbf{N}_\lambda c_1\mathrm{d}\Gamma, \mathbf{G} = -\int_{\Gamma}\left(\nabla\mathbf{N}_{f_2}\right)^T\mathbf{n}_2\mathbf{N}_\lambda c_2\mathrm{d}\Gamma\\&\mathbf{R}_1 = \int_{\Gamma_N}\mathbf{N}_{f_1}^T\left(\nabla u_1\cdot\mathbf{n}_1\right)\mathrm{d}\Gamma, \mathbf{R}_2 = \int_{\Gamma_N}\mathbf{N}_{f_2}^T\left(\nabla u_2\cdot\mathbf{n}_2\right)\mathrm{d}\Gamma\end{aligned} \tag{9}$$

3. Formulation of the edge-based gradient smoothing technique in inhomogeneous media

In this work, the standard finite element scheme in conjunction with the edge-based gradient smoothing technique is used for spatial discretization. As usual, we named the present method as the edge-based smoothed FEM (ES-FEM). Following the similar steps in several published papers about ES-FEM [44,48,51], we firstly create the related edge-based smoothing domains to implement the gradient smoothing operations. As shown in Fig. 2, the standard triangular meth is used as the background mesh, here we use the different colors to describe the different domain with different media. As a result, each edge-based smoothing domain is constructed by connecting the endpoints of the considered edge and the centroids of two neighboring elements, so each edge corresponds to one edge-based smoothing domain. For the inner edges, each smoothing domain has two smoothing sub-domains; while for the boundary edges the obtained smoothing domain only has one smoothing sub-domain.

However, for the problem domain with different media, the interface Γ between two different media should be regarded as the global boundary. Therefore, each edge along the interface corresponds to two independent smoothing domains (see Fig. 2).

Therefore, for the inner and global boundary edges the corresponding smoothed element stiffness matrix is given by [48,51]

$$\bar{\mathbf{K}}^e = \int_{\Omega_i^s}\left(\bar{\mathbf{B}}_i\right)^T\bar{\mathbf{B}}_i\mathrm{d}\Omega \tag{10}$$

in which Ω_i^s $(i = 1, 2)$ is the obtained edge-based smoothing domain, $\bar{\mathbf{B}}_i$ $(i = 1, 2)$ is the smoothed gradient matrix in the problem domain with different media.

For the edges along the interface Γ, the corresponding element stiffness matrix is given by

$$\bar{\mathbf{K}}^e = \int_{\Omega_1^s}\bar{\mathbf{B}}_1^T\bar{\mathbf{B}}_1\mathrm{d}\Omega + \int_{\Omega_2^s}\bar{\mathbf{B}}_2^T\bar{\mathbf{B}}_2\mathrm{d}\Omega \tag{11}$$

For the wave propagation in a pre-stressed membrane, the relationship between displacement u and particle velocity v is given by

$$v = -c\nabla u\cdot\mathbf{n} \tag{12}$$

in which c is the wave propagation speed.

From Eq. (12), it is seen that the particle velocity v is related to the gradient of the displacement u. In this work, the edge-based gradient smoothing operation is performed by smoothing the particle velocity v and the smoothed particle velocity can be obtained by

$$\bar{v}\left(\mathbf{x}_k\right) = \int_{\Omega_k^s}v\left(\mathbf{x}_k\right)W\left(\mathbf{x}-\mathbf{x}_k\right)\mathrm{d}\Omega \tag{13}$$

in which $W(\mathbf{x}-\mathbf{x}_k)$ is a pre-defined smoothing function given by [44]

$$W\left(\mathbf{x}-\mathbf{x}_k\right) = \begin{cases}0\mathbf{x}\notin\Omega_k^s\\1/A_s^k\mathbf{x}\in\Omega_k^s\end{cases} \tag{14}$$

in which A_s^k stands for the area of the smoothing domain.

Substituting Eq. (12) and Eq. (14) into Eq. (13), and using the divergence theorem, we have

$$\bar{v}\left(\mathbf{x}_k\right) = -\frac{c}{A_k^s}\int_{\Omega_k^s}\nabla u\mathrm{d}\Omega = -\frac{c}{A_k^s}\int_{\Gamma_k^s}u\cdot\mathbf{n}\mathrm{d}\Gamma \tag{15}$$

in which Γ_s^k is the boundary of the edge-based smoothing domain, $\mathbf{n}$ is the corresponding outward unit normal vector.

Using the usual finite element interpolation scheme, the smoothed particle velocity field can be written by

$$\bar{v}\left(\mathbf{x}_k\right) = -c\sum_{i\in M_k}\bar{\mathbf{B}}_i(\mathbf{x})u_i \tag{16}$$

in which M_k is the total number of nodes which have contributions to form the smoothed gradient matrix $\bar{\mathbf{B}}_i$, namely the involved nodes in the smoothing domain.

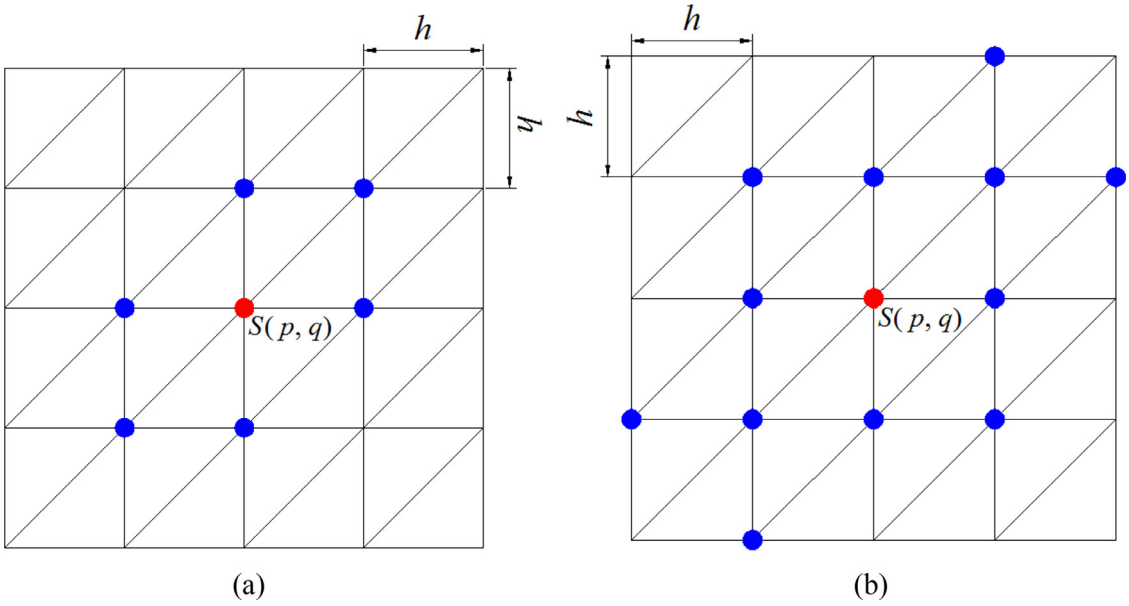

Fig. 3. The employed uniform mesh pattern and the illustration of involved nodes for dispersion analysis: (a) FEM; (b) ES-FEM.

In this work the Gauss integration scheme is used to perform the related numerical integration along the boundary of smoothing domain which consists of N_s segments, then smoothed gradient matrix $\bar{\mathbf{B}}_i$ can be obtained by

$$\bar{\mathbf{B}}_i(\mathbf{x}) = \frac{1}{A_k^s}\sum_{q=1}^{N_s}\left(\sum_{r=1}^{N_g} w_r \mathbf{N}_i(\mathbf{x})\begin{bmatrix} n_x \\ n_y \end{bmatrix}\right) \tag{17}$$

in which N_g is the number of Gauss points in each segment, the number of Gauss points is determined by the order of the used nodal shape functions, w_r is the weighting coefficients, n_x and n_y are the components of the outward normal vector.

Then the smoothed global stiffness can be obtained by assembling each smoothed element stiffness matrix as in the standard finite element scheme, namely

$$\bar{\mathbf{K}} = \sum \bar{\mathbf{K}}^{(k)} = \sum\left(\int_{\Omega_k^s} \bar{\mathbf{B}}^T \bar{\mathbf{B}} \mathrm{d}\Omega\right) = \sum\left(\bar{\mathbf{B}}^T \bar{\mathbf{B}} A_k^s\right) \tag{17}$$

in which $\bar{\mathbf{K}}^{(k)}$ is smoothed element stiffness matrix for edge k.

4. Dispersion analysis of the ES-FEM for transient wave problems

It is known that the dispersion error of the numerical solutions for transient wave propagation problems always consists of the contributions from spatial discretization and the contributions from temporal discretization. Here we firstly investigate the spatial discretization error.

4.1. Spatial discretization error

The spatial discretization error is closely related to the used mesh pattern. In this paper the uniform mesh with average nodal space h shown in Fig. 3 is used for dispersion analysis. Although the non-uniform mesh are always employed in real engineering computation, the analysis and discussion here still have great significance.

For the time independent form of the wave equation, the following matrix equation can be obtained without considering the boundary condition [56]

$$\mathbf{Ku} - k^2\mathbf{Mu} = \mathbf{0} \tag{18}$$

in which $\mathbf{u}$ is the vector of unknown solution variables, k is the exact wave number, $\mathbf{K}$ and $\mathbf{M}$ are stiffness matrix and mass matrix, respectively.

As shown in Fig. 3, for the standard FEM and the present ES-FEM model all the nodes which have contributions to form the system matrices associated with the central node $S_{(p,q)}$ (red solid node) are marked in blue solid nodes, here p and q represent the row number and column number, respectively. It is very clear to see that the number of involved nodes in ES-FEM model is much larger than that in the standard FEM model due to the additional used edge-based gradient smoothing technique.

Note that no boundary conditions are considered, so the numerical solutions corresponding to the involved nodes in Fig. 3 should have the same amplitude and can be represented by

$$\mathbf{u} = Ae^{jk_h\mathbf{n}\cdot\mathbf{x}} \tag{19}$$

in which $j = \sqrt{-1}$ and A is the amplitude of the numerical solutions and k_h is the numerical wave number, $\mathbf{n}$ is a unit vector denotes the wave propagation direction and $\mathbf{x}$ is the position vector of the considered point.

Substituting the Eq. (19) into Eq. (18), and only looking at the equation corresponding to the middle red node of a patch of elements, we can obtain [56]

$$\left(\mathbf{D}_{\text{stiff}} - k^2\mathbf{D}_{\text{mass}}\right)\mathbf{u} = \mathbf{0} \tag{20}$$

in which $\mathbf{D}_{\text{stiff}}$ and $\mathbf{D}_{\text{mass}}$ are the matrices corresponding to the system stiffness matrix $\mathbf{K}$ and system mass matrix $\mathbf{M}$.

By referring to the node distributions in Fig. 3, for the standard FEM and ES-FEM model we have

$$\begin{aligned}\mathbf{D}_{\text{stiff}}^{\text{FEM}} = {} & \mathbf{K}_{p,q}^{\text{FEM}} + \mathbf{K}_{p,q-1}^{\text{FEM}} e^{-jk_h h\cos\theta} + \mathbf{K}_{p,q+1}^{\text{FEM}} e^{jk_h h\cos\theta} + \\ & \mathbf{K}_{p-1,q-1}^{\text{FEM}} e^{jk_h h(-\cos\theta-\sin\theta)} + \mathbf{K}_{p-1,q}^{\text{FEM}} e^{jk_h h(-\sin\theta)} + \\ & \mathbf{K}_{p+1,q}^{\text{FEM}} e^{jk_h h\sin\theta} + \mathbf{K}_{p+1,q+1}^{\text{FEM}} e^{jk_h h(\cos\theta+\sin\theta)}\end{aligned} \tag{21}$$

$$\begin{aligned}\mathbf{D}_{\text{mass}}^{\text{FEM}} = {} & \mathbf{M}_{p,q}^{\text{FEM}} + \mathbf{M}_{p,q-1}^{\text{FEM}} e^{-jk_h h\cos\theta} + \mathbf{M}_{p,q+1}^{\text{FEM}} e^{jk_h h\cos\theta} + \\ & \mathbf{M}_{p-1,q-1}^{\text{FEM}} e^{jk_h h(-\cos\theta-\sin\theta)} + \mathbf{M}_{p-1,q}^{\text{FEM}} e^{jk_h h(-\sin\theta)} + \\ & \mathbf{M}_{p+1,q}^{\text{FEM}} e^{jk_h h\sin\theta} + \mathbf{M}_{p+1,q+1}^{\text{FEM}} e^{jk_h h(\cos\theta+\sin\theta)}\end{aligned} \tag{22}$$

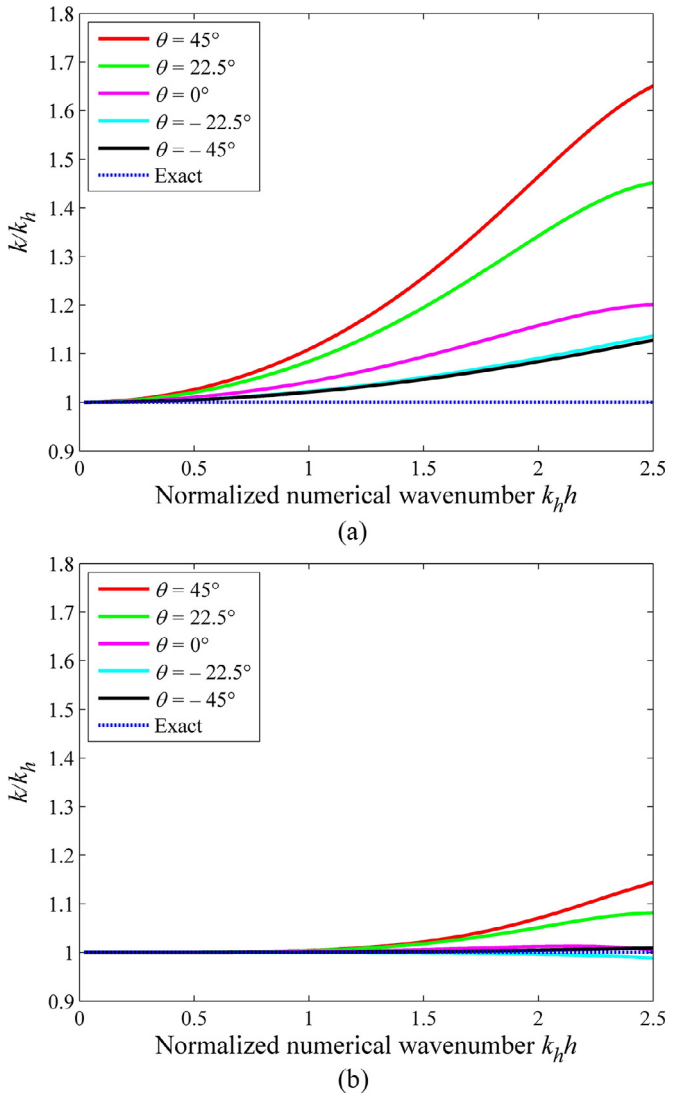

Fig. 4. The spatial dispersion properties for the standard FEM and ES-FEM in different wave propagation directions: (a) FEM; (b) ES-FEM.

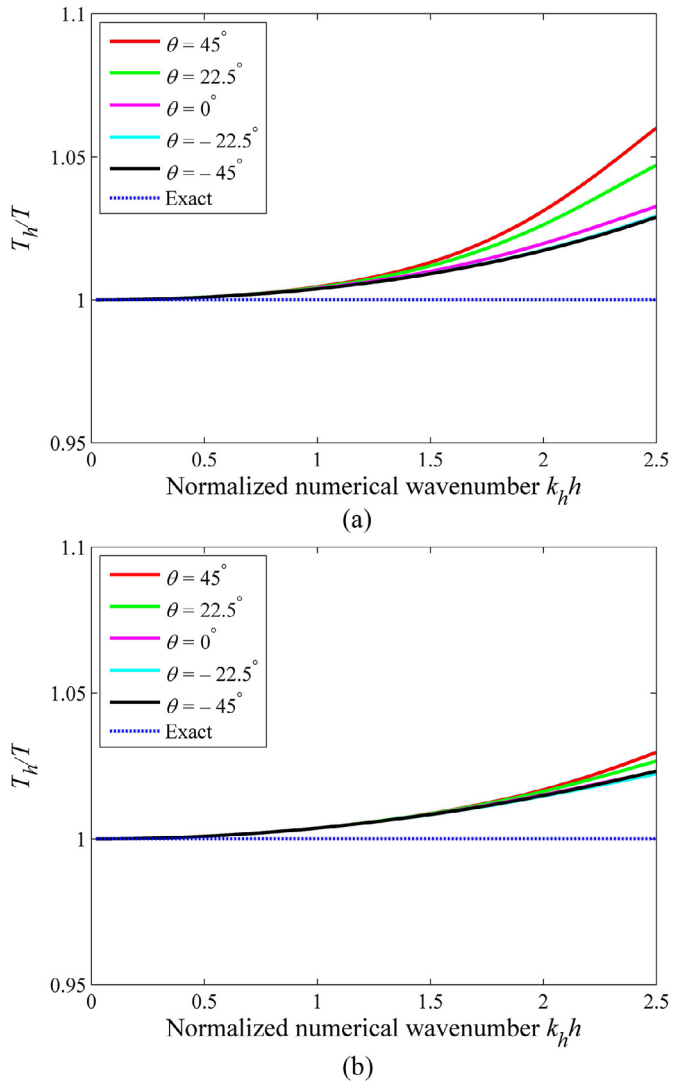

Fig. 5. The period elongation properties of the standard FEM and the present ES-FEM with Bathe time integration scheme: (a) FEM; (b)ES-FEM.

$$\begin{aligned}\mathbf{D}_{\text{stiff}}^{\text{ES-FEM}} &= \mathbf{K}_{p,q}^{\text{ES-FEM}} + \mathbf{K}_{p,q-1}^{\text{ES-FEM}} e^{-jk_h h\cos\theta} + \mathbf{K}_{p,q+1}^{\text{ES-FEM}} e^{jk_h h\cos\theta} \\ &+\mathbf{K}_{p-2,q-1}^{\text{ES-FEM}} e^{jk_h h(-\cos\theta-2\sin\theta)} + \mathbf{K}_{p+2,q+1}^{\text{ES-FEM}} e^{jk_h h(\cos\theta+2\sin\theta)} \\ &+\mathbf{K}_{p-1,q-2}^{\text{ES-FEM}} e^{jk_h h(-2\cos\theta-\sin\theta)} + \mathbf{K}_{p-1,q-1}^{\text{ES-FEM}} e^{jk_h h(-\cos\theta-\sin\theta)} + \\ &\mathbf{K}_{p-1,q}^{\text{ES-FEM}} e^{jk_h h(-\sin\theta)} + \mathbf{K}_{p-1,q+1}^{\text{ES-FEM}} e^{jk_h h(\cos\theta-\sin\theta)} + \mathbf{K}_{p+1,q-1}^{\text{ES-FEM}} e^{jk_h h(-\cos\theta+\sin\theta)} + \\ &\mathbf{K}_{p+1,q}^{\text{ES-FEM}} e^{jk_h h(\sin\theta)} + \mathbf{K}_{p+1,q+1}^{\text{ES-FEM}} e^{jk_h h(\cos\theta+\sin\theta)} + \mathbf{K}_{p+1,q+2}^{\text{ES-FEM}} e^{jk_h h(2\cos\theta+\sin\theta)} + \end{aligned} \tag{23}$$

$$\begin{aligned}\mathbf{D}_{\text{mass}}^{\text{ES-FEM}} &= \mathbf{M}_{p,q}^{\text{ES-FEM}} + \mathbf{M}_{p,q-1}^{\text{ES-FEM}} e^{-jk_h h\cos\theta} + \mathbf{M}_{p,q+1}^{\text{ES-FEM}} e^{jk_h h\cos\theta} \\ &+\mathbf{M}_{p-2,q-1}^{\text{ES-FEM}} e^{jk_h h(-\cos\theta-2\sin\theta)} + \\ &\mathbf{M}_{p+2,q+1}^{\text{ES-FEM}} e^{jk_h h(\cos\theta+2\sin\theta)} + \mathbf{M}_{p-1,q-2}^{\text{ES-FEM}} e^{jk_h h(-2\cos\theta-\sin\theta)} \\ &+\mathbf{M}_{p-1,q-1}^{\text{ES-FEM}} e^{jk_h h(-\cos\theta-\sin\theta)} + \\ &\mathbf{M}_{p-1,q}^{\text{ES-FEM}} e^{jk_h h(-\sin\theta)} + \mathbf{M}_{p-1,q+1}^{\text{ES-FEM}} e^{jk_h h(\cos\theta-\sin\theta)} + \mathbf{M}_{p+1,q-1}^{\text{ES-FEM}} e^{jk_h h(-\cos\theta+\sin\theta)} + \\ &\mathbf{M}_{p+1,q}^{\text{ES-FEM}} e^{jk_h h(\sin\theta)} + \mathbf{M}_{p+1,q+1}^{\text{ES-FEM}} e^{jk_h h(\cos\theta+\sin\theta)} + \mathbf{M}_{p+1,q+2}^{\text{ES-FEM}} e^{jk_h h(2\cos\theta+\sin\theta)} + \end{aligned} \tag{24}$$

If there exists non-trivial solutions for Eq. (20), we must have

$$\det\left(\mathbf{D}_{\text{stiff}} - k^2\mathbf{D}_{\text{mass}}\right) = \mathbf{0} \tag{25}$$

It is clear that the matrices $\mathbf{D}_{\text{stiff}}$ and $\mathbf{D}_{\text{stiff}}$ contain the numerical wave number k_h, so Eq. (25) describes the relationship between the numerical wave number k_h and exact wave number k. In other words, for any given numerical wave number k_h, we can obtain the corresponding exact wave number k using Eq. (25), then we can obtain the spatial discretization error which is defined by k/k_h.

For both the standard FEM and the present ES-FEM, Fig. 4 gives the calculated spatial dispersion error k/k_h in different wave propagation directions versus the non-dimensional wave number $k_h h/\pi$ $(= h/(\lambda_h/2))$ in which λ_h is the numerical wavelength. Obviously, the values on the horizontal axis also represents the resolution of the wave. From the spatial dispersion properties shown in the figure, it is seen that for both of the two different methods the dispersion error is very small for small non-dimensional wave numbers and will become larger with the increase of the considered non-dimensional wave number values, however, the spatial dispersion error from the present ES-FEM is clearly smaller than that from the standard FEM.

In addition, we also can find that the spatial dispersion properties of the standard FEM depend strongly on the wave propagation directions, namely the standard FEM shows significant "numerical anisotropy" issue in wave analysis. While this issue can be obviously alleviated to some extent by using the present ES-FEM. The reason for this is that the edge-based gradient smoothing operation is employed in ES-FEM, then better numerical solutions can be obtained.

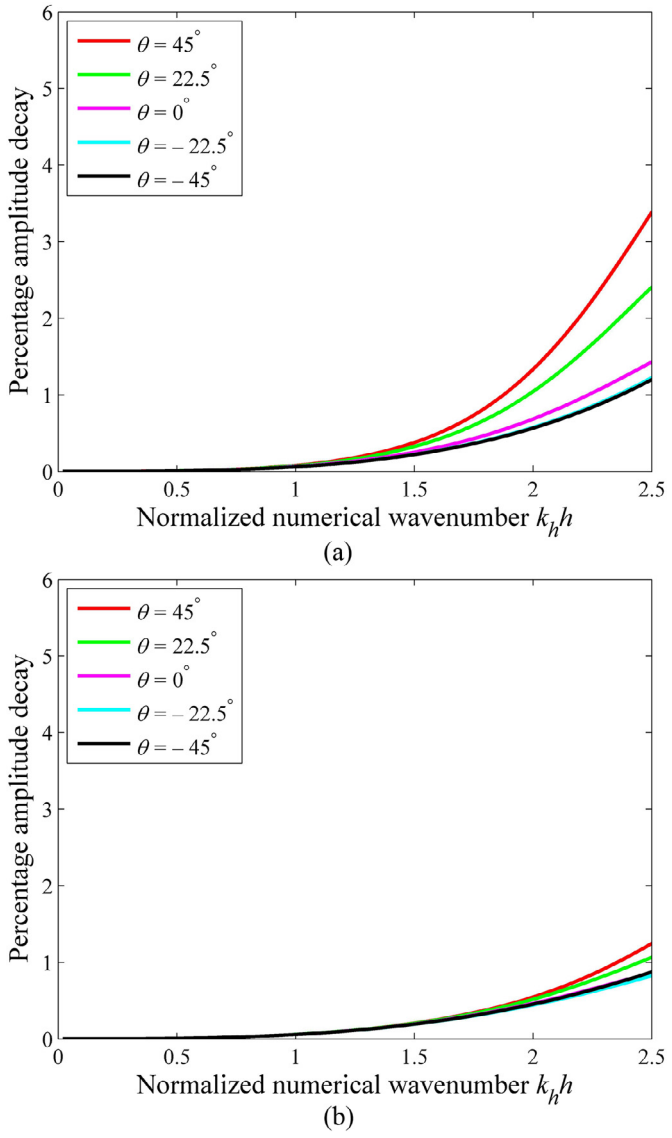

Fig. 6. The amplitude decay properties of the standard FEM and the present ES-FEM with Bathe time integration scheme: (a) FEM; (b)ES-FEM.

4.2. Temporal discretization error from the time integration

From the analysis and discussion in the previous sub-section, we have known that the calculated numerical solutions for wave problems usually suffers from the spatial dispersion error induced from the spatial discretization. In this sub-section, the temporal discretization error the present ES-FEM with Bathe time integration scheme in solving transient wave problems will be discussed and examined in details.

By using the usual finite element interpolation and without considering the boundary conditions, the general governing matrix equation for transient wave propagation problems can be written by

$$\mathbf{M}\ddot{\mathbf{u}} + c^2\mathbf{K}\mathbf{u} = \mathbf{0} \tag{26}$$

The fundamental solution to Eq. (26) has the following form

$$\mathbf{u} = Ae^{j(k\mathbf{n}\cdot\mathbf{x}-\omega_h t)} \tag{27}$$

in which ω_h denotes the numerical angular frequency.

Substituting Eq. (27) into Eq. (26) and again referring to the mesh pattern in Fig. 3, we have

$$\mathbf{D}_{\text{mass}}\ddot{\mathbf{u}} + c^2\mathbf{D}_{\text{stiff}}\mathbf{u} = \mathbf{0} \tag{28}$$

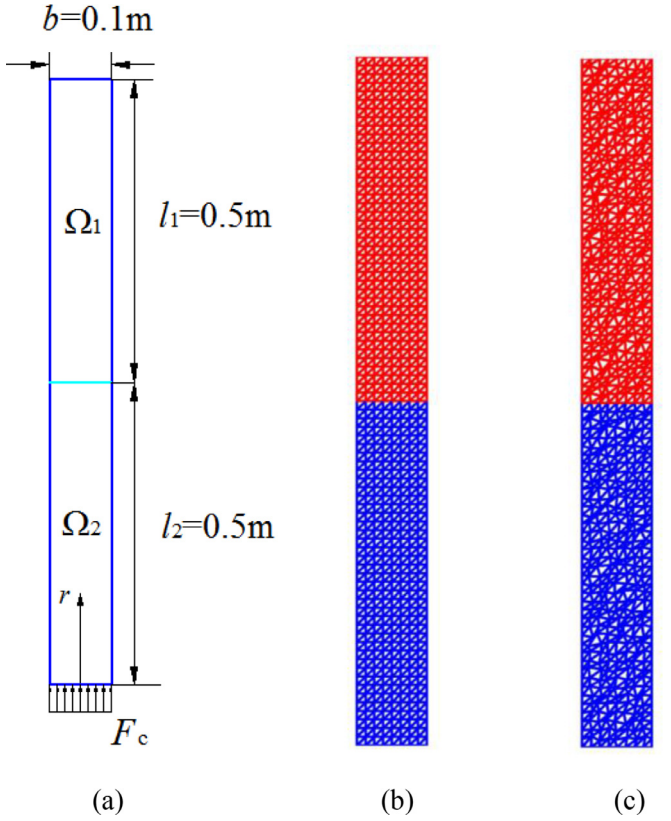

Fig. 7. The problem description and used mesh patterns for the two-dimensional tube: (a) The geometry description of the tube; (b) The used uniform mesh; (c) The used distorted mesh.

in which the matrices $\mathbf{D}_{\text{mass}}$ and $\mathbf{D}_{\text{stiff}}$ have been obtained in Eqs. (21) – (24).

Using the Bathe time integration scheme for temporal discretization [56], we have

$$\begin{cases} {}^{t+\Delta t/2}\dot{\mathbf{u}} = {}^{t}\dot{\mathbf{u}} + \frac{\Delta t}{4}\left({}^{t}\ddot{\mathbf{u}} + {}^{t+\Delta t/2}\ddot{\mathbf{u}}\right) \\ {}^{t+\Delta t/2}\mathbf{u} = {}^{t}\mathbf{u} + \frac{\Delta t}{4}\left({}^{t}\dot{\mathbf{u}} + {}^{t+\Delta t/2}\dot{\mathbf{u}}\right) \\ {}^{t+\Delta t}\dot{\mathbf{u}} = \frac{1}{\Delta t}{}^{t}\mathbf{u} - \frac{4}{\Delta t}{}^{t+\Delta t/2}\mathbf{u} + \frac{3}{\Delta t}{}^{t+\Delta t}\mathbf{u} \\ {}^{t+\Delta t}\ddot{\mathbf{u}} = \frac{1}{\Delta t}{}^{t}\dot{\mathbf{u}} - \frac{4}{\Delta t}{}^{t+\Delta t/2}\dot{\mathbf{u}} + \frac{3}{\Delta t}{}^{t+\Delta t}\dot{\mathbf{u}} \end{cases} \tag{29}$$

in which Δt is the used time step.

Using Eq. (27) and Eq. (29),Eq. (28) can be expressed by

$${}^{t+2\Delta t}\mathbf{u} - \frac{288 - 94\omega^2\Delta t^2}{144 + 25\omega^2\Delta t^2 + \omega^4\Delta t^4}{}^{t+\Delta t}\mathbf{u} + \frac{144 + 25\omega^2\Delta t^2}{144 + 25\omega^2\Delta t^2 + \omega^4\Delta t^4}{}^{t}\mathbf{u} = \mathbf{0} \tag{30}$$

Note that the unknown solution vector $\mathbf{u}$ has the fundamental solution $\mathbf{u} = Ae^{j(k\mathbf{n}\cdot\mathbf{x}-\omega_h t)}$, from Eq. (30) we can obtain the following equation [56]

$$\left(e^{-j\omega_h\Delta t}\right)^2 + me^{-j\omega_h\Delta t} + n = 0 \tag{31}$$

in which $m = -\frac{288-94\omega^2\Delta t^2}{144+25\omega^2\Delta t^2+\omega^4\Delta t^4}$ and $n = \frac{144+25\omega^2\Delta t^2}{144+25\omega^2\Delta t^2+\omega^4\Delta t^4}$, ω is exact angular frequency which can be obtained from Eq. (25).

From Eq. (31), it is easy to obtain

$$\omega_h\Delta t = j\ln\left(\frac{-m \pm \sqrt{m^2 - 4n}}{2}\right) \tag{32}$$

It is found that the numerical wave number ω_h is a complex number because there exists numerical damping effects in the Bathe time integration technique [56,57].

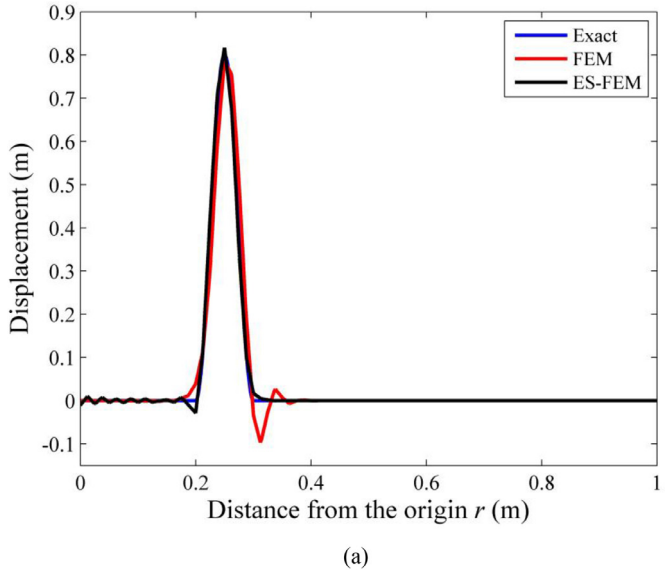

(a)

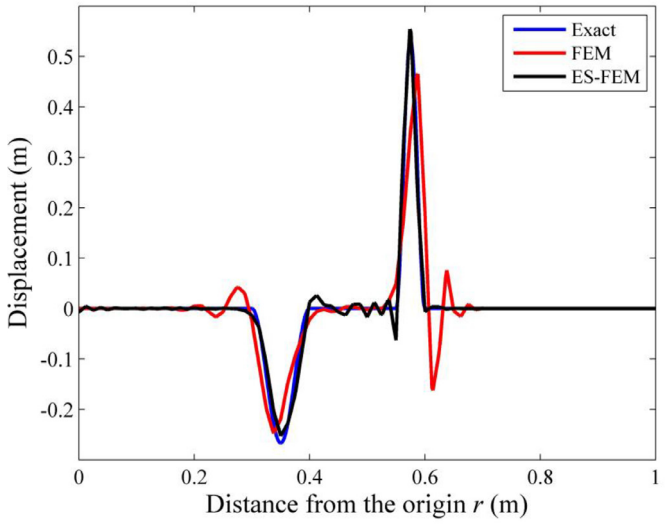

(b)

Fig. 8. The displacement results from the standard FEM and ES-FEM for the two-dimensional tube: (a) The observation time $t = 0.3$ s; (b) The observation time $t = 0.7$ s.

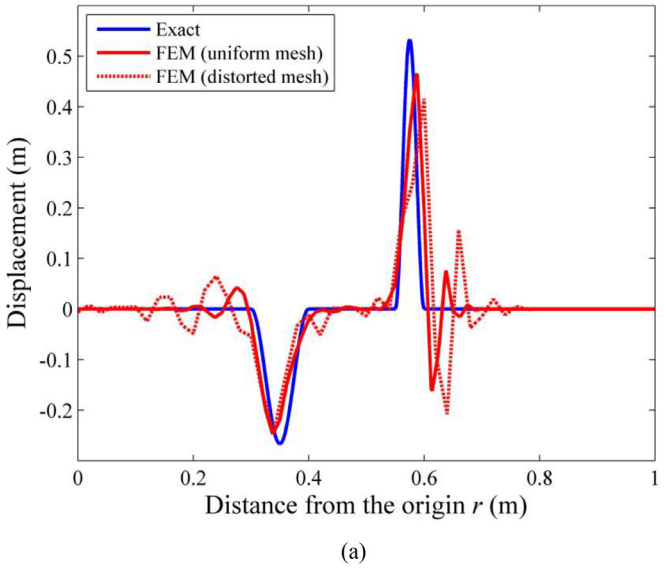

(a)

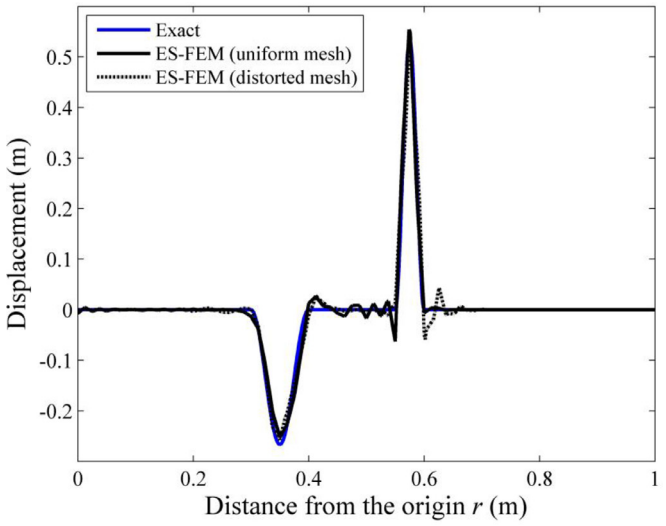

(b)

Fig. 9. The displacement results from uniform and distorted mesh at observation time $t = 0.7$ s for the two-dimensional tube: (a) FEM; (b) ES-FEM.

Here Eq. (32) can also be re-written by

$$\omega_h \Delta t = \text{Real} + j\text{Imag} \tag{33}$$

Then the complex modulus of the numerical wave solution to the general wave equation can be obtained by

$$\begin{aligned} \left|Ae^{-j\omega_h \Delta t}\right| &= \left|Ae^{-j(\text{Real}+j\text{Imag})}\right| = \left|Ae^{-j\text{Real}+\text{Imag}}\right| \\ &= \left|Ae^{\text{Imag}}\right| \cdot \underbrace{\left|e^{-j\text{Real}}\right|}_{=1} = \left|Ae^{\text{Imag}}\right| \end{aligned} \tag{34}$$

Then the percentage amplitude decay (AD) per Δt can be calculated by [57]

$$\zeta = 1 - \frac{Ae^{\text{Imag}}}{A} = \left(1 - e^{\text{Imag}}\right) \times 100\% \tag{35}$$

In Eq. (33), the real part of the parameter $\omega_h \Delta t$ corresponds to the phase position of the numerical wave solution. Note that the exact wave solution is $e^{-j\omega t}$, so the percentage period elongation (PE) of the Bathe method can be obtained by

$$\begin{aligned} \text{PE} &= \left(\frac{T_h}{T} - 1\right) \times 100\% = \left(\frac{2\pi/(\text{Real}/\Delta t)}{2\pi/\omega} - 1\right) \times 100\% \\ &= \left(\frac{\omega}{\text{Real}/\Delta t} - 1\right) \times 100\% \end{aligned} \tag{36}$$

in which T_h is the numerical wave period and T is the exact wave period.

If we use the numerical damping ratio ξ_h to describe the percentage amplitude decay as in Ref. [56], using Eq. (33) we can have

$$\xi_h = -\frac{\text{Imag}}{\text{Real}} = -\frac{\ln\left(\left|e^{-j\omega_h t_h}\right|\right)}{\text{Real}} = -\frac{1}{2}\frac{\ln\left(\left|\frac{-m \pm \sqrt{m^2-4n}}{2}\right|\right)}{\text{Real}} \tag{37}$$

Then the percentage amplitude decay per period T is obtain by [56]

$$\text{AD} = \left(1 - e^{2\pi \frac{\text{Imag}}{\text{Real}}}\right) \times 100\% = \left(1 - e^{-2\pi\xi_h}\right) \times 100\% \tag{38}$$

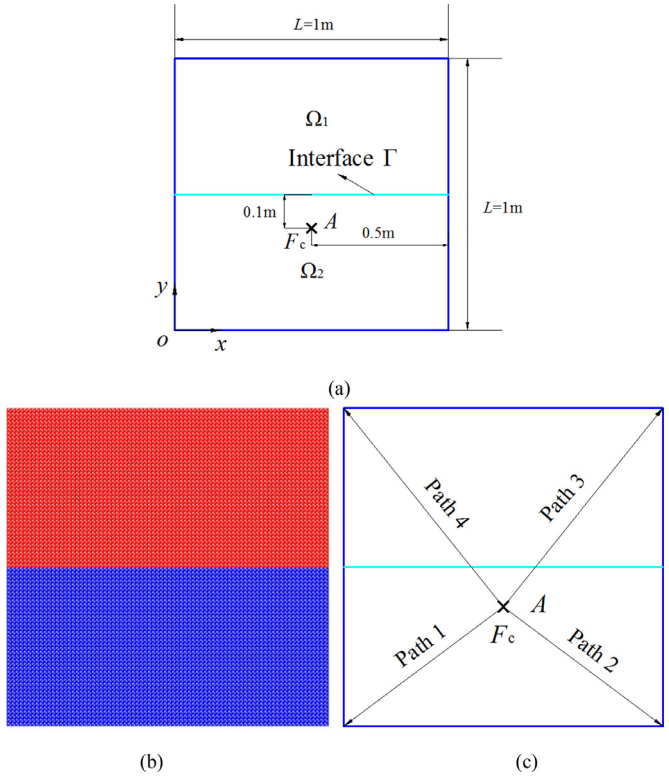

Fig. 10. The square problem domain with different media: (a) The geometry description of the considered square domain; (b) The used uniform mesh; (c) The pre-defined paths.

Finally, the total dispersion error c_h/c can be expressed by

$$\frac{c_h}{c} = \frac{\omega_h/k_h}{\omega/k} = \frac{k}{k_h}\frac{\omega_h}{\omega} = \frac{k}{k_h}\frac{T}{T_h} \tag{39}$$

From Eq. (39), it is seen that the total dispersion error of the calculated numerical solutions mainly consists of two different parts. The first part, which is defined by k/k_h, is spatial dispersion error and the second part is the temporal dispersion error which is defined by T/T_h. From Eq. (25), it is found that the spatial dispersion error is mainly determined by the used mesh pattern, while the temporal dispersion error is not only dominated by the used time integration scheme, but also influenced by the spatial dispersion error. Another interesting point is that in general the spatial dispersion error satisfies $k/k_h > 1$ and the temporal dispersion error satisfies $T/T_h < 1$. This means that these two different error components can be balanced out to some extent. Not that the obtained temporal dispersion error is related to the used time step Δt, hence for a given mesh pattern (namely for a fixed spatial dispersion error) there should exist an appropriate time step Δt to obtain very accurate numerical solutions with minimal total dispersion error for transient wave problems. However, this "optimal" time step Δt is in general not easy to obtain and this issue is still a very open question so far.

The period elongation and amplitude decay properties of the standard FEM and the present ES-FEM with Bathe time integration technique for CFL=0.3 are shown in Fig. 5 and Fig. 6. Here the pre-defined parameter is given by CFL=$c\Delta t/h$ [56,57], the values of the CFL number corresponds to the ratio of the traveled length per time step ($c\Delta t$) to the used average nodal space. From the calculated numerical results shown in the figures we can find:

1) Compared to the standard FEM, the period elongation and amplitude decay from the present ES-FEM is much smaller. The reason for this is that the ES-FEM can provide much smaller spatial dispersion error due to the used edge-based gradient smoothing operations. Note that the temporal dispersion error is also related to the spatial dispersion error, so the ES-FEM is also able to produce smaller temporal dispersion error than the standard FEM.
2) It is again found that the standard FEM clearly shows the "numerical anisotropy" issue, namely the period elongation and amplitude decay results from the standard FEM vary very much for the different wave propagation directions. Though the present ES-FEM also suffers from this issue, it can be significantly relieved to some extent thanks to the used edge-based gradient smoothing operations.

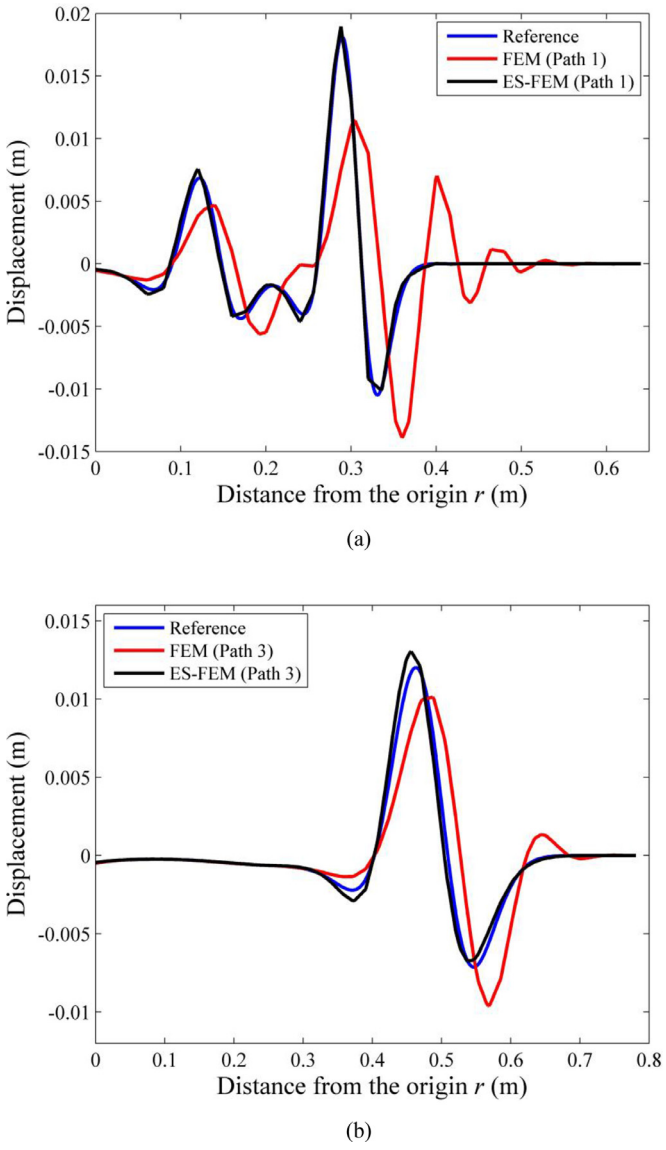

Fig. 11. The displacements calculated from the standard FEM and the ES-FEM for the two-dimensional square pre-stressed membrane at observation time t = 0.4s: (a) Path 1; (b) Path 3.

5. Numerical examples

In last section, we have detailedly discussed and analyzed the dispersion error properties (including the spatial dispersion error and temporal dispersion error) of the traditional FEM and the present ES-FEM with Bathe time integration scheme for transient wave propagation problems. It is seen that the ES-FEM indeed behaves better in reducing the numerical dispersion error than the traditional FEM. In this section, several typical numerical examples are considered to examine the performance of

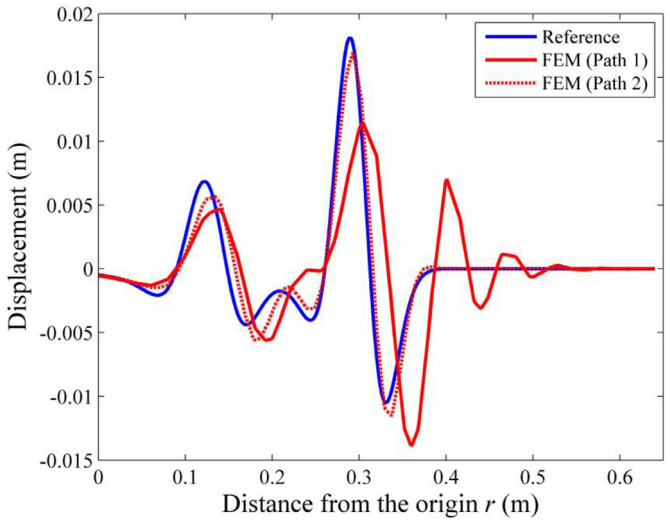

(a)

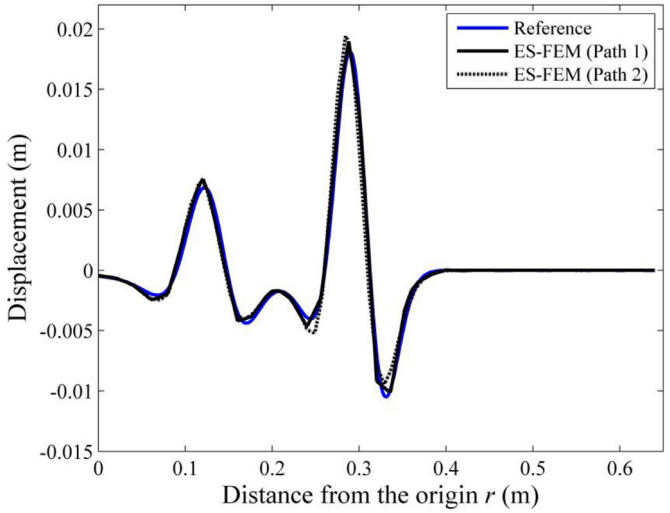

(b)

Fig. 12. The numerical solutions from different methods for the two-dimensional square pre-stressed membrane along different paths at observation time t = 0.4s: (a) FEM; (b) PES-FEM.

the present ES-FEM with Bathe time integration scheme in solving practical transient wave propagation in inhomogeneous media. It should be pointed out that all the waves (including incident, reflecting and transmitted waves) do not reach the boundary of the computational domain for the considered time, hence the non-reflecting boundary conditions (such as Dirichlet-to-Neumann map or perfect matched layer) are not required in this work.

5.1. The two-dimensional tube

The first considered numerical example is the scalar wave propagations in a two-dimensional tube with length l = 1 m and width b = 0.1 m. As shown in Fig. 7a, this tube contains two different media. The wave speeds in these two different media are c_1=0.5 m/s and c_2=1 m/s. The excitation pressure *Fc* is imposed on the bottom side of the tube. Since one of its dimensions is much smaller than the other one and all the variables don't vary along the horizontal direction, so this problem can be considered as a typical one-dimensional problem even though the problem domain is in a two dimensional space. We assume that a plane wave $u = 0.8\sin(20\pi t)$, $t \in [0, 0.05]$ is propagating in this tube. The considered problem domain is divided into uniform and distorted meshes (see Fig. 7b and Fig. 7c) with $2 \times 8 \times 80$triangular elements and the Bathe time integration technique with CFL=0.1 is employed to tackle this wave propagation problem. Both the numerical results from the standard FEM and the ES-FEM will be provided and discussed here.

Firstly, the displacement results at observation time t = 0.3 s obtained from the standard FEM and the present ES-FEM are plotted in Fig. 8a. It is seen that the standard FEM results basically agree with the exact solutions though several spurious oscillations can be found behind the wave front. However, it is obvious that the ES-FEM results are much better than the FEM results and agree very well with the exact solutions. Furthermore, we also calculated the displacement results at observation time t = 0.7 s using the FEM and ES-FEM (see Fig. 8b), the first peak in the figure is the reflected waves and the second peak is the waves penetrating the interface of the two different media. We can find that the performance of the ES-FEM in predicting the physical behaviors of the waves is much better than the traditional FEM and more accurate numerical solutions can be obtained.

In more details, we also investigated the sensitivity of the present ES-FEM with Bathe time integration scheme to mesh distortion in solving transient wave propagation problems. The used uniform mesh and distorted mesh are shown in Fig. 7b and Fig. 7c. The displacement results from FEM and ES-FEM at observation time t = 0.7 s are plotted Fig. 9. We can see that more spurious oscillations can be seen in the FEM results when using distorted mesh. However, the ES-FEM is less sensitive to the mesh distortion than the standard FEM, and very good solutions can still be obtained even if the distorted mesh is used. The reason for this is that the edge-based gradient smoothing technique is used in ES-FEM, so it is more suitable to describe real displacement field.

5.2. The two-dimensional square domain

As shown in Fig. 10a, the second considered 2D problem is the scalar wave propagations in a square pre-stressed membrane (length L = 1 m) with two different media. The wave speed in this two different media are c_1 =2 m/s and c_2=1 m/s. The uniform triangular mesh with $2 \times 80 \times 80$ elements is employed to discretize the considered problem domain (see Fig. 10b). A concentrated force F_c is imposed at point A. The used concentrated force here is a Ricker wavelet and defined by [56]

$$F_c = 0.4\left[1 - 2\pi^2 f_p^2 (t - t_s)^2\right] \exp\left(-\pi^2 f_p^2 (t - t_s)^2\right) \tag{40}$$

in which the peak frequency f_p=10 Hz is used here and the time shift t_s=0.1 s.

In order to clearly discuss and analyze the numerical results from the standard FEM and the present ES-FEM, several pre-defined paths are shown in Fig. 10c. Firstly, for CFL=0.1, the displacements calculated from the standard FEM and the ES-FEM along Path 1 at observation time t = 0.4 s are plotted in Fig. 11a. The higher peaks in the figure is the original incident wave from the source and the lower peak is the wave reflected by the interface of the two different media. Note that the corresponding exact solutions to this problem is not easy to obtain, here the numerical solutions from the traditional FEM with a very fine mesh are also provided as the reference solutions. From the results shown in the figure, we can observe that the ES-FEM solution is clearly much better than the standard FEM solution and is closer to the reference solution. In addition, we also calculated the numerical solutions along Path 3 at observation time t = 0.4 s using the FEM and ES-FEM (see Fig. 11b). Likewise, the similar points can be found.

Fig. 12a gives the FEM solutions along different paths at observation time t = 0.4 s. It is known that the exact solutions along Path 1 and Path 2 should be identical due to the symmetry of this problem. However, we can find that the FEM solutions are obviously different along the different paths. The reason for this is that the standard FEM shows clear numerical anisotropic property even if the considered media are

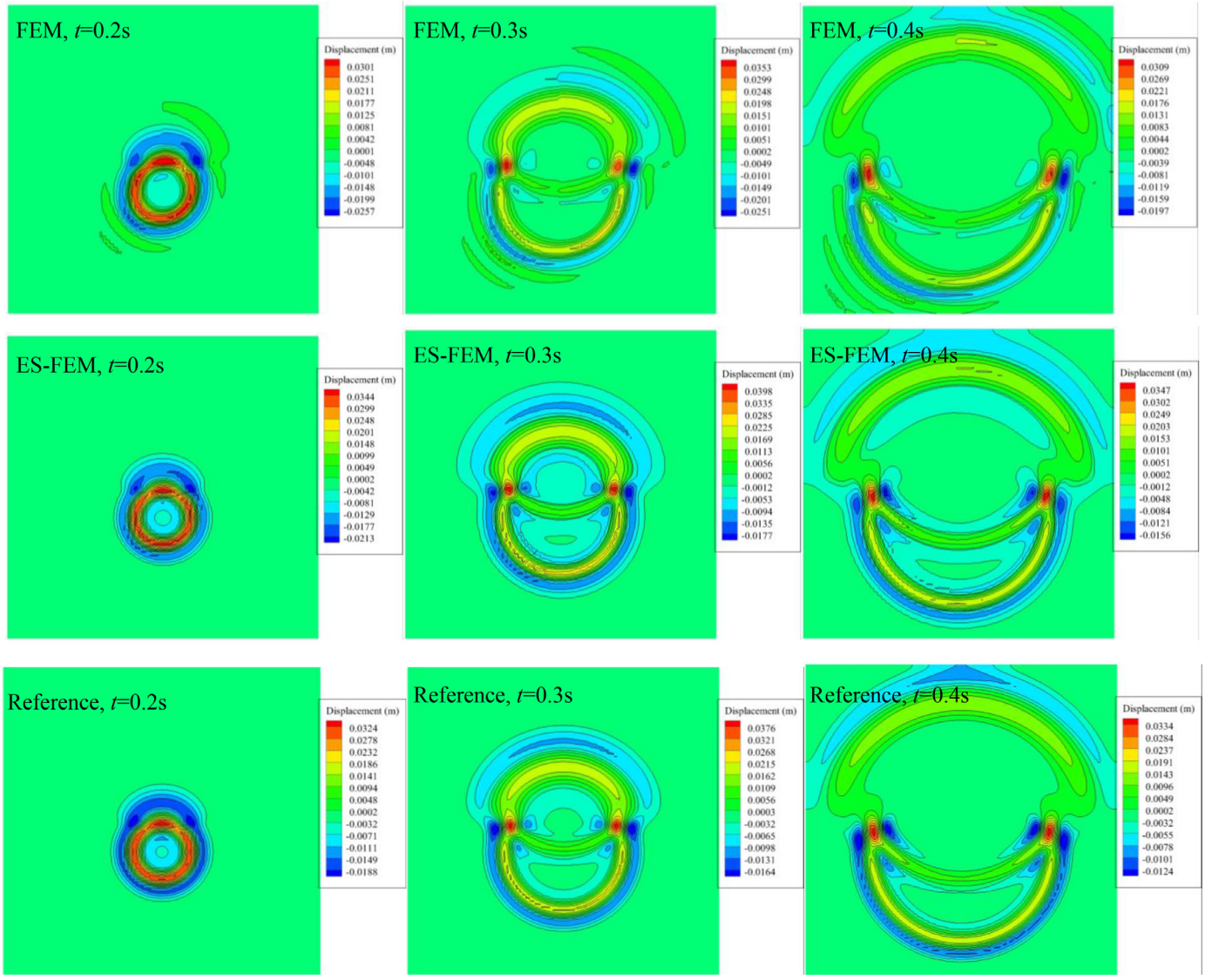

Fig. 13. Snapshots of the displacement distributions from different methods for the two-dimensional square pre-stressed membrane at different observation times.

isotropic. For comparison, the corresponding numerical solutions from the ES-FEM are also calculated and shown in Fig. 12b. It is seen that the numerical anisotropic effects can be significantly suppressed by the present ES-FEM, namely the corresponding numerical solutions from the ES-FEM are almost same in the different wave propagation directions.

Fig. 13 presents several snapshots of the displacement distributions from the different methods at different observation times. The reference solutions are also presented in the figure for comparison. It is clearly seen that the ES-FEM solutions are closer to the reference solutions and numerical dispersion error from the ES-FEM is much smaller than that from the standard FEM, hence the ES-FEM solutions are smoother and better than the FEM ones.

5.3. The two-dimensional scalar wave scattering by a circular object

As shown in Fig. 14, the third numerical example we considered here is still the scalar wave propagation in a square pre-stressed membrane problem domain. However, in this case the whole problem domain contains four circular regions; the exterior and interior domain of the circular regions are different media. The wave source is at the center of the square domain and the excitation force is still a Ricker wavelet with magnitude 0.4, peak frequency f_p=10 Hz and time shift t_s=0.1 s. Due to the symmetry of this considered problem, only the domain $V = [0, 1] \times [0, 1]$ is modelled in the calculation process. The wave speeds in these two considered media are c_1=2 m/s and c_2=1 m/s.

The square problem domain is divided into standard triangular mesh with average meshsize $h = 0.016$ m (see Fig. 14). For the convenience of detailedly discussing and comparing the numerical solutions, a predefined line is plotted in Fig. 14. Firstly, for a fixed CFL=0.1, we calculated the displacement solutions at observation time $t = 0.4$ s using the standard FEM and ES-FEM along the direction $\theta = 45^\circ$ (see Fig. 14) and the results are shown in Fig. 15a. The reference solutions in the figure are still from the FEM with a very fine mesh. It is easy to see that there exist spurious oscillations in the FEM solutions, while the ES-FEM solutions are obviously better.

Then the displacement solutions from the FEM and ES-FEM at observation time $t = 0.8$ s are also calculated and plotted in Fig. 15b to clearly see how the incident wave is affected by the interface of the two different media. In Fig. 15b, the lower peak is the waves reflected by the interface and the higher peak is the transmitted waves. We can find that many spurious oscillations occur in the FEM solutions. While the ES-FEM can lead to more accurate solutions which are closer to the reference solutions, so both the reflected and transmitted waves can be relatively accurately predicted.

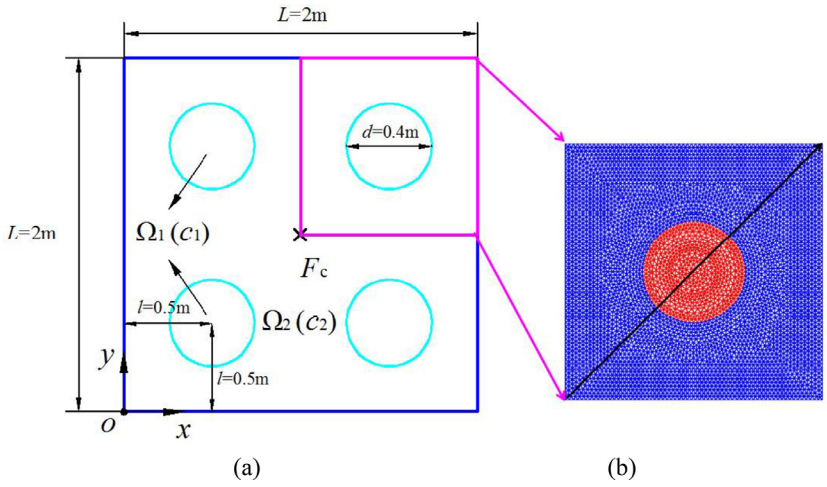

Fig. 14. The two-dimensional scalar wave scattering by circular objects: the problem description and the used triangular mesh.

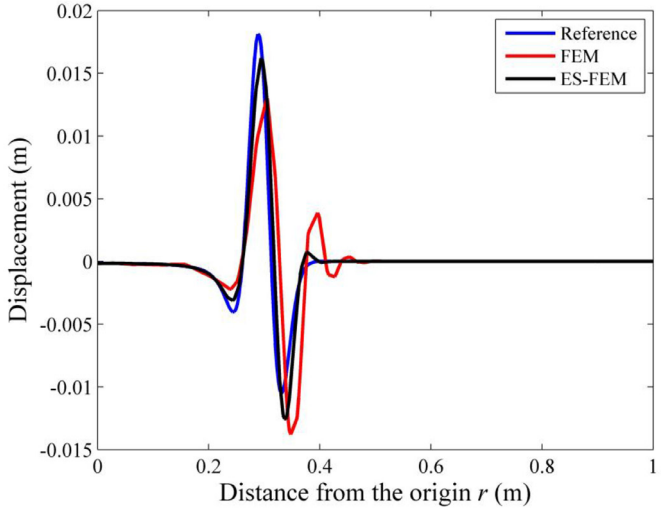

Fig. 15. The displacement solutions from the FEM and ES-FEM for the two-dimensional scalar wave scattering problem at two observation times (a) $t = 0.4$ s; (b) $t = 0.8$ s.

6. Concluding remarks

In this work the edge-based smoothed FEM (ES-FEM) is combined with the Bathe time integration scheme to solve the transient wave propagation problems in inhomogeneous media. The ES-FEM is used for spatial discretization and the Bathe time integration method is used for time discretization. In the ES-FEM, the edge-based gradient smoothing technique is employed to provide an appropriate system stiffness of the considered problem, so the spatial dispersion error can be effectively controlled. Due to the numerical dissipation effects in the Bathe time integration method, the spurious short wavelength modes in the total numerical solution can be effectively suppressed, hence smaller temporal dispersion error can be obtained. The numerical examples show that the present ES-FEM with Bathe time integration method works very well in solving transient wave problems and much smaller numerical dispersion error (including the spatial dispersion error and temporal dispersion error) can be obtained for transient wave problems compared to the traditional FEM.

In addition, the present method can produce almost the same numerical solutions with good accuracy in the different wave propagation directions, while the traditional FEM suffers from the “numerical anisotropy” issue and the calculated numerical solutions strongly depend on the wave propagations; what’s more, for the transient wave problems the present method also shows lower sensitivities to the quality of the used meshes than the standard FEM, so very reliable numerical solutions can still be reached even if very distorted meshes are employed. Due to these attractive features, the present ES-FEM with Bathe time integration scheme can be regarded as a very good alternative to the traditional FEM for solving transient wave propagation problems.

Declaration of Competing Interest

None.

Acknowledgments

The authors wish to express their gratitude to the National Natural Science Foundation of China (grant number 51809208), Fundamental Research Funds for the Central Universities (grant number WUT: 2019IVB012) and the China Postdoctoral Science Foundation (grant number 2018M632866 and 2018M642940).

References

[1] Bathe KJ. Finite element procedures. 2nd editor. Watertown (MA): Prentice Hall; 2014.
[2] Zienkiewicz OC, Taylor RL. The finite element method for solid and structural mechanics. Elsevier; 2005.

[3] Wu X, Yun M, Wang M, Liu C, Li K, Qin X, et al. Self-imaging in multi-walled carbon nanotube arrays at visible wavelengths. Carbon N Y 2016;108:47–51.
[4] Mullen R, Belytschko T. Dispersion analysis of finite element semidiscretizations of the two-dimensional wave equation. Int J Numer Meth Eng 1982;18:11–29.
[5] Deraemaeker A, Babuška I, Bouillard P. Dispersion and pollution of the FEM solution for the Helmholtz equation in one, two and three dimensions. Int J Numer Meth Eng 1999;46:471–99.
[6] Chai YB, Gong ZX, Li W, Li TY, Zhang QF, Zou ZH, Sun YB. Application of smoothed finite element method to two-dimensional exterior problems of acoustic radiation. Int J Comput Methods 2018;15:1850029.
[7] Chai YB, Li W, Gong ZX, Li TY. Hybrid smoothed finite element method for two dimensional acoustic radiation problems. Appl Acoust 2016;103:90–101.
[8] You XY, Li W, Chai YB. Dispersion analysis for acoustic problems using the point interpolation method. Eng Anal Bound Elem 2018;94:79–93.
[9] Noh G, Ham S, Bathe KJ. Performance of an implicit time integration scheme in the analysis of wave propagations. Comput Struct 2013;123:93–105.
[10] Babuška I, Ihlenburg F, Paik ET, Sauter SA. A generalized finite element method for solving the Helmholtz equation in two dimensions with minimal pollution. Comput Methods Appl Mech Engrg 1995;128:325–59.
[11] Chai YB, You XY, Li W. Dispersion Reduction for the Wave Propagation Problems Using a Coupled "FE-Meshfree" Triangular Element. Int J Comput Methods 2020. doi:10.1142/S0219876219500713.
[12] Steffens LM, Parés N, Díez P. Estimation of the dispersion error in the numerical wave number of standard and stabilized finite element approximations of the Helmholtz equation. Int J Numer Methods Eng 2011;86:1197–224.
[13] Wu TW. Boundary element acoustics: fundamentals and computer codes. Southampton: WIT Press; 2000.
[14] Li JP, Chen W, Qin QH. A modified dual-level fast multipole boundary element method based on the Burton–Miller formulation for large-scale three-dimensional sound field analysis. Comput Meth Appl Mech Eng 2018;340:121–46.
[15] Li JP, Chen W, Fu ZJ, Qin QH. A regularized approach evaluating the near-boundary and boundary solutions for three-dimensional Helmholtz equation with wideband wavenumbers. Appl Math Lett 2019;91:55–60.
[16] Chen LC, Li XL. A complex variable boundary element-free method for the Helmholtz equation using regularized combined field integral equations. Appl Math Lett 2020;101:106067.
[17] Fu ZJ, Yang LW, Xi Q, Liu CS. A boundary collocation method for anomalous heat conduction analysis in functionally graded materials. Comput Math Appl 2020. doi:10.1016/j.camwa.2020.02.023.
[18] Wang F, Fan CM, Hua Q, Gu Y. Localized MFS for the inverse Cauchy problems of two-dimensional Laplace and biharmonic equations. Appl Math Comput 2020;364:124658.
[19] Li JP, Chen W, Qin QH, Fu ZJ. A modified multilevel algorithm for large-scale scientific and engineering computing. Comput Math Appl 2019;77:2061–76.
[20] Wang F, Gu Y, Qu W, Zhang C. Localized boundary knot method and its application to large-scale acoustic problems. Comput Meth Appl Mech Eng 2020;361:112729.
[21] Wang F, Wang C, Chen Z. Local knot method for 2D and 3D convection-diffusion-reaction equations in arbitrary domains. Appl Math Lett 2020;105:106308.
[22] Chen LC, Li XL. An efficient meshless boundary point interpolation method for acoustic radiation and scattering. Comput Struct 2020;229:106182.
[23] Fu ZJ, Zhang J, Li PW, Zheng JH. A semi-Lagrangian meshless framework for numerical solutions of two-dimensional sloshing phenomenon. Eng Anal Bound Elem 2020;112:58–67.
[24] Xu YY, Zhang GY, Zhou B, Wang HY, Tang Q. Analysis of acoustic radiation problems using the cell-based smoothed radial point interpolation method with Dirichlet-to-Neumann boundary condition. Eng Anal Bound Elem 2019;108:447–58.
[25] Fu ZJ, Zhang J, Li PW, Zheng JH. A semi-Lagrangian meshless framework for numerical solutions of two-dimensional sloshing phenomenon. Eng Anal Bound Elem 2020;112:58–67.
[26] Fu ZJ, Xie ZY, Ji SY, Tsai CC, Li AL. Meshless generalized finite difference method for water wave interactions with multiple-bottom-seated-cylinder-array structures. Ocean Eng 2020;195:106736.
[27] Lin J, Xu Y, Zhang Y. Simulation of linear and nonlinear advection–diffusion–reaction problems by a novel localized scheme. Appl Math Lett 2020;99:106005.
[28] Yao LY, Wu F, Wu G. Numerical study of exterior acoustic problems using a novel finite element-least square point interpolation method with perfectly matched layer. Eng Anal Bound Elem 2019;102:87–96.
[29] Qu W, Fan CM, Li XL. Analysis of an augmented moving least squares approximation and the associated localized method of fundamental solutions. Comput Math Appl 2020;80:13–30.
[30] Komatitsch D, Barnes C, Tromp J. Simulation of anisotropic wave propagation based upon a spectral element method. Geophysics 2000;65:1251–60.
[31] Seriani G, Oliveira SP. Dispersion analysis of spectral element methods for elastic wave propagation. Wave Motion 2008;45:729–44.
[32] He ZC, Li E, Liu GR, Li GY, Cheng AG. A mass-redistributed finite element method (MR-FEM) for acoustic problems using triangular mesh. J Comput Phys 2016;323:149–70.
[33] Li E, He ZC. Optimal balance between mass and smoothed stiffness in simulation of acoustic problems. Appl Math Model 2019;75:1–22.
[34] Li E, He ZC. Stability and accuracy improvement for explicit formulation of time domain acoustic problems. Eng Anal Bound Elem 2017;83:217–28.
[35] You XY, Li W, Chai YB. A truly meshfree method for solving acoustic problems using local weak form and radial basis functions. Appl Math Comput 2020;365:124694.
[36] Chai YB, Cheng C, Li W, Huang Y. A hybrid Finite element-Meshfree method based on partition of unity for transient wave propagation problems in homogeneous and inhomogeneous media. Appl Math Model 2020;85:192–209.
[37] Chai YB, Li W, Gong ZX, Li TY. Hybrid smoothed finite element method for two-dimensional underwater acoustic scattering problems. Ocean Eng 2016;116:129–41.
[38] Wu F, Hu M, Chen K, Yao LY, Ju ZG, Sun X. Stochastic interval analysis for structural natural frequencies based on stochastic hybrid perturbation edge-based smoothing finite element method. Eng Anal Bound Elem 2019;103:41–50.
[39] Li W, Zhang QF, Gui Q, Chai YB. A Coupled FE-Meshfree Triangular Element for Acoustic Radiation Problems. Int J Comput Methods 2020. doi:10.1142/S0219876220410029.
[40] Harari I, Hughes TJR. Galerkin/least-squares finite element methods for the reduced wave equation with non-reflecting boundary conditions in unbounded domains. Comput Methods Appl Mech Eng 1992;98:411–54.
[41] Liu GR. Mesh free methods: moving beyond the finite element method. CRC press; 2002.
[42] Liu GR. An overview on meshfree methods: for computational solid mechanics. Int J Comput Methods 2016;13:1630001.
[43] Zienkiewicz OC. Achievements and some unsolved problems of the finite element method. Int J Numer Methods Eng 2000;47:9–28.
[44] Liu GR, Nguyen-Thoi, Smoothed T. finite element method, New York: Taylor and Francis Group; 2010. CRC Press.
[45] Cui XY, Hu X, Wang G, Li GY. An accurate and efficient scheme for acoustic-structure interaction problems based on unstructured mesh. Comput Meth Appl Mech Eng 2017;317:1122–45.
[46] Li W, Gong ZX, Chai YB, Cheng C, Li TY, Zhang QF. Hybrid gradient smoothing technique with discrete shear gap method for shell structures. Comput Math Appl 2017;74:1826–55.
[47] Jiang C, Zhang ZQ, Gao GJ, Liu GR. A modified immersed smoothed FEM with local field reconstruction for fluid–structure interactions. Eng Anal Bound Elem 2019;107:218–32.
[48] He ZC, Li GY, Zhong ZH, Cheng AG, Zhang GY, Li E, Liu GR. An ES-FEM for accurate analysis of 3D mid-frequency acoustics using tetrahedron mesh. Comput Struct 2012;106:125–34.
[49] He ZC, Li GY, Zhong ZH, Cheng AG, Zhang GY, Liu GR, Li E, Zhou Z. An edge-based smoothed tetrahedron finite element method (ES-T-FEM) for 3D static and dynamic problems. Comput Mech 2013;52:221–36.
[50] Li E, He ZC, Xu X. An edge-based smoothed tetrahedron finite element method (ES--T-FEM) for thermomechanical problems. Int J Heat Mass Tran 2013;66:723–32.
[51] Chai YB, You XY, Li W, Huang Y, Yue Z, Wang MS. Application of the edge-based gradient smoothing technique to acoustic radiation and acoustic scattering from rigid and elastic structures in two dimensions. Comput Struct 2018;203:43–58.
[52] He ZC, Liu GR, Zhong ZH, Wu SC, Zhang GY, Cheng AG. An edge-based smoothed finite element method (ES-FEM) for analyzing three-dimensional acoustic problems. Comput Metheds Appl Mech Eng 2009;199:20–33.
[53] Hu X, Cui XY, Zhang Q, Wang G, Li GY. The stable node-based smoothed finite element method for analyzing acoustic radiation problems. Eng Anal Bound Elem 2017;80:142–51.
[54] Wang G, Cui XY, Feng H, Li GY. A stable node-based smoothed finite element method for acoustic problems. Comput Meth Appl Mech Eng 2015;297:348–70.
[55] Li W, Chai YB, Lei M, Li TY. Numerical investigation of the edge-based gradient smoothing technique for exterior Helmholtz equation in two dimensions. Comput Struct 2017;182:149–64.
[56] Kim KT, Zhang LB, Bathe KJ. Transient implicit wave propagation dynamics with overlapping finite elements. Comput Struct 2018;199:18–33.
[57] Kim KT, Bathe KJ. Transient implicit wave propagation dynamics with the method of finite spheres. Comput Struct 2016;173:50–60.